Micromechanical modeling of the elastic behavior of unidirectional CVI SiC/SiC composites

Camille Chateau, L. Gélébart, Michel Bornert, Jérôme Crépin

To cite this version:

Camille Chateau, L. Gélébart, Michel Bornert, Jérôme Crépin. Micromechanical modeling of the elastic behavior of unidirectional CVI SiC/SiC composites. International Journal of Solids and Structures, 2015, 58, pp.322-334. 10.1016/j.ijsolstr.2014.11.020 . hal-01120398

HAL Id: hal-01120398
https://enpc.hal.science/hal-01120398v1

Submitted on 25 Feb 2015

Micromechanical modeling of the elastic behavior of unidirectional CVI SiC/SiC composites

C.Chateau[a,b], L.Gélébart[a*], M.Bornert[b], J.Crépin[c]

[a] *CEA, DEN, DMN, SRMA, 91191 Gif-sur-Yvette Cedex, France*
[b] *Université Paris-Est, Laboratoire Navier (UMR 8205), CNRS, ENPC, IFSTTAR, F-77455 Marne-la-Vallée*
[c] *Mines ParisTech, Centre des matériaux (CNRS UMR 7633), BP 87, 91003 Evry Cedex, France*

* Corresponding author: lionel.gelebart@cea.fr tel: +33 1 69 08 16 78, fax: +33 1 69 08 71 30

Abstract

The elastic behavior of SiC/SiC composite is investigated at the scale of the tow through a micromechanical modeling taking into account the heterogeneous nature of the microstructure. The paper focuses on the sensitivity of transverse properties to the residual porosity resulting from the matrix infiltration process. The full analysis is presented stepwise, starting from the microstructural characterization to the study of the impact of pore shape and volume fraction. Various Volume Elements (VEs) of a virtual microstructure are randomly generated. Their microstructural properties are validated with respect to an experimental characterization based on high definition SEM observations of real materials, using various statistical descriptors. The linear elastic homogenization is performed using finite elements calculations for several VE sizes and boundary conditions. Important fluctuations of the apparent behavior, even for large VEs, reveal that scales are not separated. Nevertheless, a homogeneous equivalent behavior is estimated by averaging apparent behaviors of several VEs smaller than the Representative Volume Element (RVE). Therefore, the impact of the irregular shape of the pores on the overall properties is highlighted by comparison to a simpler cylindrical porous microstructure. Finally, different matrix infiltration qualities are simulated by several matrix thicknesses. A small increase in porosity volume fraction is shown to potentially lead to an important fall of transverse elastic moduli together with high stress concentrations.

Keywords : Ceramic matrix composites (CMC); Elasticity; Finite element; Porosity; Pore shape.

***NOTICE**: This is the author's version of a work that was accepted for publication in International Journal of Solids and Structures. Changes resulting from the publishing process, such as editing, corrections, structural formatting, and other quality control mechanisms may not be reflected in this document. Changes may have been made to this work since it was submitted for publication. A definitive version was subsequently published in Int. J. Solids Struct. 58 (2015), http://dx.doi.org/10.1016/j.ijsolstr.2014.11.020.*

1. Introduction

The prospect of using silicon carbide for nuclear applications is now seriously considered because of its good behavior under severe conditions. In order to avoid the limits due to the brittle nature of the monolithic SiC, while retaining its performances at high temperature and after irradiation, the material is studied under its composite form (Katoh et al., 2007). Particularly, the last generations of SiC/SiC composites currently developed are based on near-stoichiometric SiC fibers (Hi-Nicalon S or Tyranno-SA3 fibers) which present very stable properties (Sauder and Lamon, 2007; Sha et al., 2004). Several processes are still under consideration to deposit the SiC matrix within the woven fibrous preform (Naslain, 2004) and improve the thermo-mechanical behavior of the composite. Yet, the Chemical Vapor Infiltration (CVI) is promising since it produces a highly pure and near-stoichiometric β-SiC matrix (Deck et al., 2012; Igawa et al., 2005), which is required to limit degradation under radiation. Nevertheless, this process does not allow a perfect infiltration of the composite and leads to an inter- and intra-tow residual porosity. It has been observed that a minimal porosity volume fraction – resulting of a very long infiltration – is necessary to get the best mechanical performances (Deck et al., 2012; Hironaka et al., 2002). In fact, a too low density would lead to an important loss in elastic and strength properties, the size and distribution of voids having effects on matrix cracks propagation. Thus, in the context of the development of a multi-scale predictive model of the mechanical behavior of SiC/SiC composites (Chateau et al., 2014; Gélébart et al., 2010), the influence of porosity is a critical aspect to study. We focus in this paper on the elastic behavior of the tow, which is the intermediate scale of the multi-scale microstructure, in between the scale of the individual fiber and that of the woven structure. Given its unidirectional geometry, a specific attention will be paid to the transverse mechanical properties.

The effect of fiber arrangements on the micro-scale behavior of composites has been largely discussed in the literature using analytical models or numerical simulation, especially for unidirectional fiber-reinforced polymers. It is shown that the transverse overall behavior may depend on the non-uniform distribution of fibers (Aghdam and Dezhsetan, 2005; Melro et al., 2012; Wongsto and Li, 2005), in addition to elementary material properties. But the inter-fiber distances also impact the local stress state, which is directly related to the onset and the propagation of microscopic damage events (Knight et al., 2003; Maligno et al., 2009; Romanowicz, 2010; Trias et al., 2006). Thus, a realistic representation is crucial to adequately predict overall behavior and damage evolution. This issue is particularly true for CVI SiC/SiC microstructure whose heterogeneity is mainly coming from the porosity, as SiC CVI matrix and 3rd generation fibers have similar elastic properties. Indeed, the sensitivity of overall elastic properties to porosity was evaluated numerically and analytically for simplified pore geometries (ellipsoids) in laminate composite (Huang and Talreja, 2005), showing in particular a void shape effect. Similarly, the size and spatial arrangement of pore with circular cross section were numerically shown to impact the fracture strength in ceramics (Keleş et al., 2013). In the case of CVI microstructures, it is necessary to additionally consider the irregular shape of the pores. The analytical model developed in (Novak et al., 2002; Tsukrov and Novak, 2002) highlights a loss of accuracy on effective elastic properties estimates if this irregularity is neglected. This result was confirmed by a preliminary numerical model of SiC/SiC microstructures (Gélébart and Colin, 2009).

So the purpose in the present work is to describe the macroscopic and local elastic behavior of the tow, taking into account the heterogeneous distribution of its constituents. This will be achieved by a numerical homogenization of the mechanical behavior of a virtual microstructure. In addition to provide statistical results, the effects of microstructural changes, like matrix thickness, may be predicted by this approach. The computations are performed on so-called Volume Elements (VEs) of the virtual microstructure. A first method to generate a VE would be to arrange fibers so that their distribution optimally respects one statistical descriptor of the real microstructure (Zeman and Sejnoha, 2001), such as volume fraction. So the convergence of apparent properties to overall mechanical properties may be fast, but their fluctuations are under-estimated. These variations may however impact the composite behavior at the upper scale especially when considering the onset of damage which is driven by extreme local stresses. In order to preserve the random nature of the microstructure, VEs are here chosen to be as realistic as possible, satisfying several statistical descriptors. Then VEs need to be generated in large numbers, so that microstructural properties correspond to the real ones on average (Kanit et al., 2003). Therefore, an extensive microstructural characterization is necessary to validate the virtual microstructure. It is based on several statistical descriptors for fibers and porosity distribution. The full microstructural analysis is presented in section 2, together with the numerical procedures to generate the virtual microstructure and perform the mechanical simulations. The results of the mechanical homogenization performed on various VEs are discussed in section 3, addressing the Representative Volume Element (RVE) issue. Although non-separated scales issues are pointed out, the homogeneous equivalent behavior is estimated, to quantify the effects of the porosity morphology and volume fraction on both the transverse overall elastic stiffness and the local stress distribution within fibers and matrix.

2. Material and methods

2.1. Generation of a virtual microstructure

2.1.1. Microstructural observation

The material under investigation is a 2D woven (0/90) composite, provided by Snecma SPS. It is made from woven tows of 3rd generation SiC fibers (Hi-Nicalon S, ~500 fibers per tow), on which a pyrocarbon interphase (PyC, 100 nm thickness) and the SiC matrix are deposited using the CVI process (Figure 1b). In order to statistically characterize its microstructure, high definition micrographs of a polished section of the composite have been recorded with a Field Emission Gun Scanning Electron Microscope (FEG-SEM). Six tows, like the one presented in Figure 1a, were randomly chosen in the sample section and were focused on their transverse plane. Stitched images built from several high resolution images (1 pixel ≈ 0.07x0.07 μm^2) are used to get accurate statistical data about fibers and porosity distributions using image analysis. Note that full 3D analyses of the microstructures, based on X-Rays micro-computed tomography (Chateau et al., 2011), have shown that the variations of the pore sections along the fiber direction are small. They are neglected in the present study focused on the influence of the transverse geometry of the tows. Fibers and pores have been successively extracted using an image processing based on morphological operations on thresholded images, as illustrated in Figure 1c and Figure 1d. As shown in Figure 1a, the peripheral part of the tow is mainly made of a thick matrix layer (~25 µm), unlike the central part where the matrix layer surrounding fibers is much thinner (~3 µm) resulting in a higher porosity. The present study is focused on the central part of the tow where the highly heterogeneous microstructure is likely to induce an anisotropic behavior together with high stress concentrations. The shapes of the analyzed areas are similar for the six observed tows, with areas ranged from 0.051 to 0.068 mm^2.

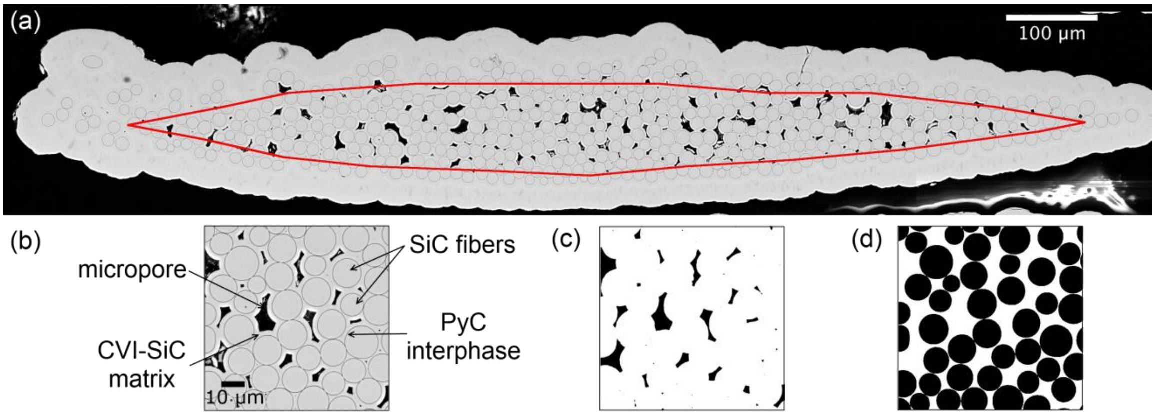

Figure 1: FEG-SEM micrograph (back-scattered electrons mode) of a transverse section of a tow; the region of interest (ROI) is outlined in red (a); zoom on the microstructure (b); extraction of pores (c) and fibers (d) by image processing.

Because fiber sections are not perfect disks, the fiber radius R_i is defined from the disk having the same area $S_i = \pi R_i^2$ than the section of the fiber i. Fiber radii range from 3 µm to 10.5 µm with an average estimated to 6.3 µm (Figure 2). As reported in Table 1, the mean fiber surface fraction S_f is rather high (63.5%). It leads to a 6.6% porosity fraction S_p with a matrix deposit thickness which ranges between 1 µm and 5 µm. Differences between the six investigated tows are noteworthy since fiber and porosity surface fractions range respectively from 59% to 70% and from 4% to 8%. A statistical characterization of fiber and pore patterns will be discussed hereafter together with the comparison to the proposed virtual microstructure (section 2.2).

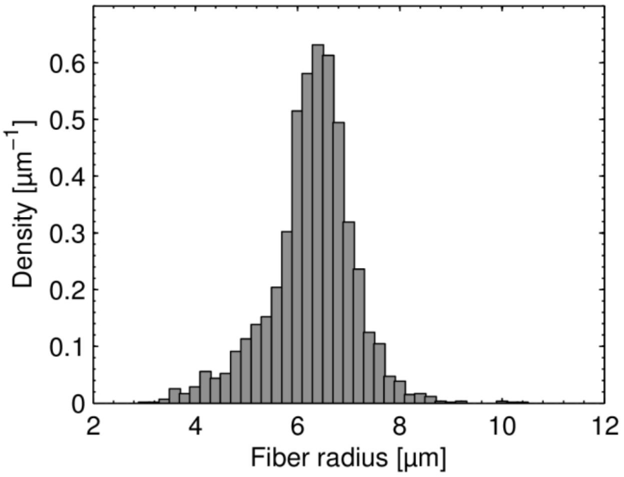

Figure 2 : Distribution of fiber radii in the six observed tows.

2.1.2. Virtual microstructure

The virtual microstructure is based on a random generation of fiber positions. Because of the high fiber surface fraction, the usual Random Sequential Adsorption model (RSA (Feder, 1980; Hinrichsen et al., 1986; Widom, 1966)) used in a preliminary study (Chateau et al., 2010; Gélébart and Colin, 2009), is no more suitable because it is limited to a 55% fiber volume fraction (when fibers with a constant diameter are used). Therefore, the chosen approach is based on collective rearrangement methods, initially developed to simulate random packing of particles (He et al., 1999; Jodrey and Tory, 1985; Nolan and Kavanagh, 1993; Yang et al., 1996). In addition to lead to the highest surface fractions, these methods are also appropriate for particles with random sizes. The used algorithm follows the model proposed by He et al. (He et al., 1999), as was already done in (Trias, 2005) in a similar context.

Each square VE (side length L, area A) is extracted from a bigger square area A_0, so that side effects due to the rearrangement method are limited and fiber fragments, whose center is located outside the VE, are taken into account. The used side length for A_0 is $L_0 = L + l_s$, where l_s is ten times as long as the maximum measured fiber radius. The number of fiber centers N_0 in A_0 is drawn from a Poisson distribution with parameter λ_0. The probability to have k fiber centers in the domain A_0 is given by equation (1), where $\lambda_0 = \lambda_{exp} L_0^2$ and λ_{exp} is the fiber center surface density experimentally measured (Table 1).

$$P(N_0 = k) = \frac{\lambda_0^k}{k!} \exp(-\lambda_0) \tag{1}$$

Initial locations of all N_0 fibers are randomly distributed in the domain A_0 following a uniform distribution. A radius R_i is randomly chosen consistently with the experimental radius distribution (Figure 2) and assigned to each fiber center i. Center positions are then rearranged until no fiber overlaps using the algorithm detailed in appendix A. To avoid trouble during the meshing of the geometry, a small distance e between fibers is added (e =0.05 µm).

The final geometry is meshed from fiber positions and diameters using the Salome platform[1]. The matrix thickness is assumed to be constant within the tow. It is estimated to 2.05 µm so that the mean porosity surface fraction fits in average the one evaluated from the experimental characterization. Thus, several VEs of various sizes may be generated. Note that no constraint of periodicity was applied on the VEs boundary to preserve the random nature of the microstructure.

2.2. Statistical characterization and validation

Both real and virtual microstructures have been quantitatively characterized using several statistical descriptors. Experimental data based on the six investigated tows is compared to simulation data based on 53 VEs of 192 µm side length (the total number of fibers N_{tot} is reported in Table 1). Because of the CVI process, the pores distribution is directly linked to the fibers distribution. Thus, the latter is characterized and compared to experimental observations below, before validating the porosity distribution.

2.2.1. Fibers distribution descriptors

Several statistical descriptors are usually used to characterize the fiber centers spatial distribution (Matsuda et al., 2003; Melro et al., 2008; Romanov et al., 2013; Vaughan and McCarthy, 2010). First, we focus on first-order descriptors that rely on the Voronoi tessellation based on the fiber centers and which characterize the short distance fiber interactions. In order to avoid side effects, the Voronoi tessellations were computed either over the whole tow or the domain A_0, taking all neighbors in account for peripheral fibers in the regions of interest. In addition to Voronoi cell areas (A_V), mean neighbor (center to center) distances (d_N) and nearest neighbor distances (d_{NN}) were estimated. Neighboring fibers

---

[1] Open source integration platform for numerical simulation, http://www.salome-platform.org.

where defined assuming they share a Voronoi cell side with the fiber considered. Fiber diameters were taken into account through local surface fraction S_{fl} (defined as the ratio of the fiber area to that of corresponding Voronoi cell) and inter-fiber distances d_N^f and d_{NN}^f.

Furthermore, second order descriptors allow one to analyze the fiber center pattern over larger distances. Known as one of the most informative descriptors (Pyrz, 1994a), the Ripley's $K(r)$ function is defined as the average number of points at a distance smaller than r from an arbitrary selected point of the pattern, divided by the point density. In order to avoid edge effects due to the finite size of the observed area A, the Ripley's corrected estimate (Ripley, 1977) is used and defined by :

$$K(r) = \frac{A}{N^2}\sum_{k=1}^{N}\frac{I_k(r)}{w_k} \tag{2}$$

where N is the number of points (i.e. fiber centers) lying in the analyzed area A, $I_k(r)$ stands for the number of points located in the circle (2D case) of center the point k and radius r, and w_k is the proportion of the circle circumference included in A.

The radial distribution function g (also known as pair distribution function) is also widely used to analyze the randomness of a point distribution. It is related to the probability to have a fiber center lying in a circular ring $\Omega_i(r)$ of radius r, thickness dr and centered on a reference point of the pattern, (Matsuda et al., 2003; Melro et al., 2008), which is given by:

$$2\pi r\lambda g(r)dr = \frac{1}{N}\sum_{i=1}^{N} n_i(r) \tag{3}$$

where N still stands for the total number of points, λ is the number of points per unit area and $n_i(r)$ is the number of points within the circular ring $\Omega_i(r)$ of center the point i. It can be demonstrated that g derives from the K function (Pyrz, 1994b) (equation (4)). This definition will be used to compute $g(r)$ (Buryachenko et al., 2003; Ghosh et al., 1997; Oh et al., 2006; Segurado and Llorca, 2002).

$$g(r) = \frac{1}{2\pi r}\frac{dK(r)}{dr} \tag{4}$$

These second order descriptors both characterize patterns in comparison to the Poisson set for which $K(r)$ and $g(r)$ are respectively equal to πr^2 and 1. While related, K and g functions show distinct characteristics (Pyrz, 1994b). Different patterns, together with local disturbances, may be distinguished using K function: a $K(r)$ function above the Poisson distribution curve would indicate the existence of clusters in the patterns, while it would stay below for patterns that exhibit some stronger regularity. Alternatively, the radial distribution function g describes the frequency of occurrences of neighbor distances: $g(r) > 1$ (and in particular local maxima) indicates that corresponding distances are more frequent than in a random pattern (and conversely for $g(r) < 1$, or local minima).

2.2.2. Experimental validation

Microstructural characteristics (fiber density λ, fiber and porosity surface fractions) are reported in Table 1 together with first-order descriptors for both experimental and simulated microstructures. First, the random fiber generation algorithm is validated as it leads to the correct fiber surface fraction. Note that the mean fiber density does not perfectly match the targeted one (i.e. the experimental one) because of slight side effects. However, these are neglected since there is no impact on the fiber surface fraction noticed. Furthermore, first-order descriptors fit well both in average and regarding their fluctuations (reflected by the relative standard deviation RSD defined as the ratio of the standard deviation to the average value). In fact, the heterogeneity and non-regularity of the microstructure should be noticed, particularly regarding the distribution of inter-fiber distances (d_N^f and d_{NN}^f) that will directly be related to the porosity heterogeneity. In spite of a small discrepancy on d_{NN}^f due to possible negative values among experimental data (fiber sections are not perfect circles), the short distance fiber interaction is well reproduced in the simulated microstructure. In particular, the prescription of the minimal distance e seems to have a limited effect on this descriptor.

			Experimental	Simulation
N_{tot}			1858	9915
λ		[mm^{-2}]	5200	5080
S_f		[%]	63.5	63.8
S_p		[%]	6.56	6.65
A_V	Avg.	[µm²]	197	198
	RSD		0.24	0.15
S_{fl}	Avg.	[%]	64	64
	RSD		0.22	0.20
d_N	Avg.	[µm]	15.3	15.4
	RSD		0.13	0.09
d_N^f	Avg.	[µm]	2.81	2.80
	RSD		0.57	0.38
d_{NN}	Avg.	[µm]	12.4	12.7
	RSD		0.10	0.10
d_{NN}^f	Avg.	[µm]	0.31	0.44
	RSD		1.19	1.23

Table 1 : Comparison of microstructural characteristics and first-order descriptors of fiber patterns in average (Avg . : average value, RSD : relative standard deviation) for real and simulated microstructures.

Besides, second order descriptors presented in Figure 3 are also in a good agreement between experimental and simulated microstructures. Both Ripley's K functions naturally exhibit a first almost stair-shaped part for short distances corresponding to fiber diameters. Both plots come then close to the perfect random pattern, keeping a tiny degree of regularity. Though it is difficult to notice, experimental observations seem to exhibit a little more regularity than simulations at large distances. This is likely to emerge from peripheral fibers in some observed tows that are more constrained by the weave. The virtual fiber distribution is finally also validated with respect to the radial distribution function g. A small shift is still observed probably because of non-circular fiber sections in the experimental pattern. Nevertheless, both functions show identical peaks position and intensity (the first one corresponding to the mean fiber diameter) and tend to unity, meaning a statistically homogeneous distribution with no order at long distances.

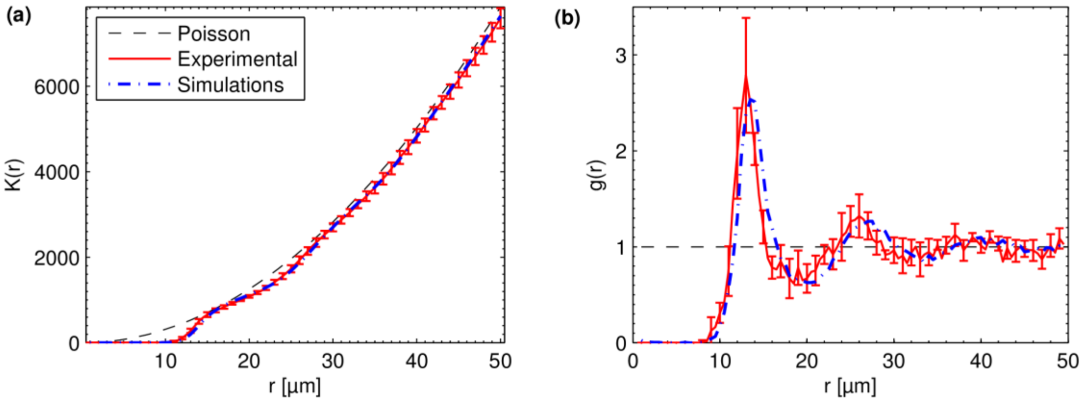

Figure 3: Comparison of spatial distribution of fibers: (a) second-order intensity function K and (b) radial distribution function g. Errorbars stand for the dispersion between the six observed tows.

As we concentrate in this work on the effect of porosity and its morphological features on the mechanical behavior, pores need to be representative of the real microstructure. The pores distribution in the virtual microstructure is compared to the experimental one in Figure 4 both in terms of numbers of pores (through normalized histograms of pore areas) and surface fraction. First of all, Figure 4 shows that the representative fiber distribution naturally leads to a good agreement for pores distribution between simulations and observations. The pore area distributions are similar (Figure 4a) with small pores (≤10 µm²) representing a large proportion of porosity, and few pores having a large area (≥100 µm²). Nevertheless, these small pores represent only a tiny part (less than 5%, see in Figure 4b) in the total porous surface.

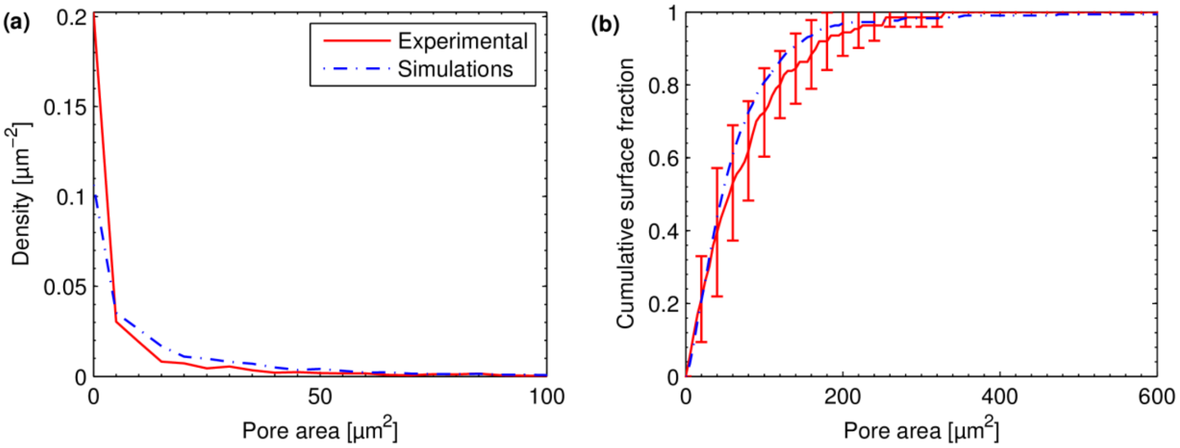

Figure 4 : (a) Mean distribution of pore areas (centered on pore areas ranging from 0 to 100 µm²), (b) Cumulative surface fraction versus pore areas. Errorbars stand for the dispersion between the six observed tows.

A sharper analysis of the graphs shows small discrepancies concerning extreme pore areas. First, the smallest ones (≤5 µm²) are half as many in the simulations as in the observations, corresponding to a reduced pore density in the virtual microstructure (0,004 pores/µm² compared to 0,007 pores/µm²). In fact, because the matrix thickness is supposed to be constant in the simulations, small empty spaces between fibers may be clogged. On the contrary, in the real microstructure, a thinner matrix in those spaces reveals a finer porosity. But, the effect of this difference on the mechanical behavior should be negligible considering the minor proportion of these small pores in the porosity. Second, the largest pores (>500 µm²) are missing in the six observed tows. Indeed, because the pores distribution is highly heterogeneous, the tail-end of the distribution is more likely to be correctly described by the large number of simulations with large areas than by the six investigated tows, which are not sufficient to be representative of such low probabilities. This assumption has been tested with a complementary observation of the same composite section, showing a few pores with large areas (until about 700 µm²) in other tows. Therefore, the simulated distribution is probably closer to the converged one, explaining the small gap observed in Figure 4b.

In short, the random generation process leads to a virtual microstructure representative of the real material. It provides an efficient tool for a statistical analysis of the mechanical behavior of the composite, since it allows one to easily generate a large number of VEs.

2.3. Mechanical homogenization

2.3.1. Finite element modeling

In order to compute the elastic overall properties by FE calculations, a 2D mesh composed of triangular elements (characteristic length ≈ 1 µm) is built for each VE using a mesh generator (Netgen1D2D) available in the Salome platform (Figure 5). The mesh is automatically refined in areas where dimensions are to small compared to the global fineness. Pores in contact with the VE boundaries have to be meshed, so that boundary conditions can be applied (especially periodic boundary conditions). A very low artificial stiffness is assigned to approximate porosity (null stiffness). This approximation is not required for the pores located inside the VE which are simply not meshed. The 3D mesh is finally built extruding the 2D mesh. In fact, the microstructure is assumed to be invariant along the fiber direction since the porosity slowly evolves in this direction. Though, a 3D mesh is used to compute all coefficients of the stiffness tensor.

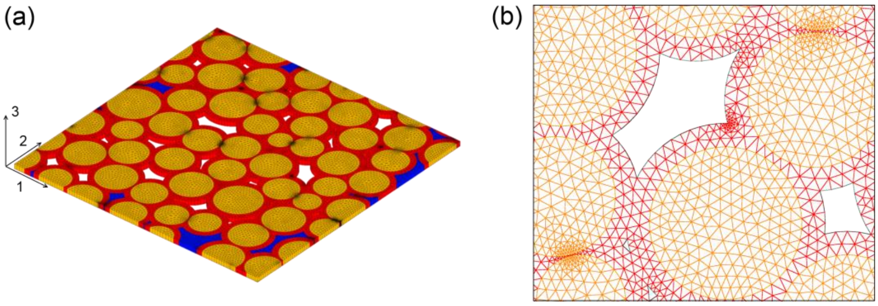

Figure 5 : (a) Typical FE mesh of a VE with matrix in red and meshed porosity in blue and (b) zoom of the mesh.

Fibers and matrix are supposed to be linearly elastic and isotropic, with an identical Poisson's ratio of 0.18. Young's moduli assigned to fibers and matrix, respectively equal to 354 GPa and 404 GPa, both derive from tensile tests performed on single fibers (Colin and Gélébart, 2008; Sauder and Lamon, 2007) and microcomposites (Colin and Gélébart, 2008; Michaux et al., 2007). Note that the elastic behavior of the solid phase (both matrix and fibers) of the composite is similar to a homogeneous media, since the contrast between the properties of fibers and the matrix are low (E_m/E_f =1.14). Hence, the main heterogeneity within the unit-cell is related to the distribution of pores (infinite contrast). Finally, very low stiffness properties (10 MPa Young's modulus) are assigned to the porous elements, with the same Poisson's ratio. This value proved to be small enough to have a negligible effect on the results of the simulations.

2.3.2. Apparent behavior

First, the apparent stiffness tensor $\boldsymbol{C}_{mech}^{app}$ of a VE Ω is defined as the 4th order tensor which links the volume averages of local strains and stresses:

$$\langle \boldsymbol{\varepsilon} \rangle = \frac{1}{|\Omega|}\int_{\Omega} \boldsymbol{\varepsilon}\, dV \,, \langle \boldsymbol{\sigma} \rangle = \frac{1}{|\Omega|}\int_{\Omega} \boldsymbol{\sigma}\, dV \tag{5}$$

$$\langle \boldsymbol{\sigma} \rangle = \boldsymbol{C}_{mech}^{app} : \langle \boldsymbol{\varepsilon} \rangle \tag{6}$$

These relations have to be satisfied for a sufficient number of independent loading conditions, associated with some particular boundary conditions as described in next section, so that $\boldsymbol{C}_{mech}^{app}$ may be fully determined. The apparent behavior can also be defined as the 4th order tensor linking the volume average strain tensor to the volume average of the energy density, again for a sufficiently large set of loading conditions, as follows:

$$\frac{1}{2}\,\langle \boldsymbol{\varepsilon} : \boldsymbol{C} : \boldsymbol{\varepsilon} \rangle = \frac{1}{2} \langle \boldsymbol{\varepsilon} \rangle : \boldsymbol{C}_{ener}^{app} : \langle \boldsymbol{\varepsilon} \rangle \tag{7}$$

where $\boldsymbol{C}$ is the local stiffness tensor. This definition ensures the symmetry of $\boldsymbol{C}_{ener}^{app}$, while it might not be the case with the first definition of $\boldsymbol{C}_{mech}^{app}$. The Hill condition given in equation (8) ensures the equivalence of the two definitions of $\boldsymbol{C}^{app}$, when this condition is satisfied by the local fields $\boldsymbol{\sigma}$ and ε associated to all loading conditions used to identify the apparent tensors of moduli.

$$\langle \boldsymbol{\sigma} \rangle : \langle \boldsymbol{\varepsilon} \rangle = \langle \boldsymbol{\sigma} : \boldsymbol{\varepsilon} \rangle \tag{8}$$

More precisely, all coefficients of the tensor are obtained by applying at least six independent loading cases (i.e. resulting in six linearly independent macroscopic stresses or strains). Solving the systems (9) and (10) leads to respectively identify $\boldsymbol{C}_{mech}^{app}$ and $\boldsymbol{C}_{ener}^{app}$, where I(or J) refers to a particular load case.

$$\langle \boldsymbol{\sigma} \rangle^{I} = \boldsymbol{C}_{mech}^{app} : \langle \boldsymbol{\varepsilon} \rangle^{I}, \forall \mathrm{I} \in [1,6] \tag{9}$$

$$\langle \boldsymbol{\sigma}^{I} : \boldsymbol{\varepsilon}^{J} \rangle = \langle \boldsymbol{\varepsilon} \rangle^{I} : \boldsymbol{C}_{ener}^{app} : \langle \boldsymbol{\varepsilon} \rangle^{J}, \forall (\mathrm{I},\mathrm{J}) \in [1,6]^2 \tag{10}$$

2.3.3. Boundary conditions

The apparent stiffness tensor depends on the particular boundary conditions applied on the VE boundaries to perform the calculation of the local fields. Boundary conditions preferably have to satisfy the Hill condition (equation (8)), which can equivalently be written at the boundary of the VE:

$$(\boldsymbol{t}(\boldsymbol{x}) - \langle \boldsymbol{\sigma} \rangle \cdot \boldsymbol{n}) \cdot (\boldsymbol{u}(\boldsymbol{x}) - \langle \boldsymbol{\varepsilon} \rangle \cdot \boldsymbol{x}) = 0, \forall \boldsymbol{x} \in \partial\Omega \tag{11}$$

where $\boldsymbol{t}$, $\boldsymbol{u}$, and $\boldsymbol{n}$ respectively refer to the traction, displacement and outward normal vectors.

Among many possible choices, some are of particular interest. The kinetic uniform boundary conditions (KUBC, equation (12)) and the static uniform boundary conditions (SUBC, equation (13)) naturally satisfy equation (11).

$$\boldsymbol{u}(\boldsymbol{x}) = \langle \boldsymbol{\varepsilon} \rangle \cdot \boldsymbol{x}, \forall \boldsymbol{x} \in \partial\Omega \tag{12}$$

$$\boldsymbol{t}(\boldsymbol{x}) = \langle \boldsymbol{\sigma} \rangle \cdot \boldsymbol{n}, \forall \boldsymbol{x} \in \partial\Omega \tag{13}$$

The periodic boundary conditions (PBC, equation (14)), where $\boldsymbol{L}$ refers to the periodicity vectors, is also easily shown to satisfy the Hill condition.

$$\boldsymbol{u}(\boldsymbol{x}+\boldsymbol{L}) = \boldsymbol{u}(\boldsymbol{x}) + \langle \boldsymbol{\varepsilon} \rangle \cdot \boldsymbol{L}\,; \boldsymbol{t}(\boldsymbol{x}+\boldsymbol{L}) = -\boldsymbol{t}(\boldsymbol{x}), \forall \boldsymbol{x} \in \partial\Omega \tag{14}$$

So called Mixed Boundary Conditions (MBC) are such that either traction or displacement boundary conditions are prescribed on complementary components at the boundaries of the VE, so that equation (11) is also satisfied; various choices are possible (Bornert et al., 2001). These four kinds of boundary conditions lead to distinct estimates of the apparent stiffness of a given finite VE. When the VE is large enough (then called the RVE), the apparent behavior no longer depends on the boundary conditions, nor the statistical realization. This limit, when it exists, determines the homogeneous equivalent behavior (or effective behavior $\boldsymbol{C}^{eff}$).

As shown by (Hazanov and Huet, 1994), SUBC and KUBC provide – for a single VE – the lower and upper bounds of any apparent stiffness tensor obtained with MBC :

$$\boldsymbol{C}_{SUBC}^{app} \leq \boldsymbol{C}_{MBC}^{app} \leq \boldsymbol{C}_{KUBC}^{app} \tag{15}$$

In case of a perfect periodic media for which the selected VE would be a unit cell, PBC would directly lead to $\boldsymbol{C}^{eff}$. When the microstructure is not periodic, PBC provide an estimate of the apparent stiffness also bounded by SUBC and KUBC estimates (Bornert et al., 2001):

$$\boldsymbol{C}_{SUBC}^{app} \leq \boldsymbol{C}_{PBC}^{app} \leq \boldsymbol{C}_{KUBC}^{app} \tag{16}$$

Here, the choice of boundary conditions is restricted by the VE geometry which is non-periodic and presents porosity connected to the boundary. Thus, SUBC are useless because they would require prescribing non null stress vectors to peripheral pores. The obtained SUBC lower bound may then be very low and not significant, given the extremely high deformation of boundary pores. Displacement controlled boundary conditions are then required to generate meaningful apparent properties if square VEs are to be considered. An alternative would be to consider non square VEs, with boundaries not intersecting the pores, which is possible as long as the porosity is closed. We refer to (Salmi et al., 2012) for such an approach which has however not been followed here.

A specific set of boundary conditions included in the set of MBCs – namely the "orthogonal mixed uniform boundary conditions" - was introduced by (Hazanov and Amieur, 1995), where the traction vector is imposed in one (or two) macroscopic direction(s) and the displacement is imposed in two (or one) orthogonal direction(s). However, it requires limitations on the VE and the loading to satisfy the Hill condition. Indeed the microstructure must be at least orthotropic and shear loadings cannot be applied, so the apparent stiffness tensor cannot be fully determined (Hazanov, 1998). To deal with these restrictions – mainly the second one – a special set of mixed boundary conditions called "periodic compatible mixed boundary conditions" was defined by (Pahr and Zysset, 2008) for six independent strain load cases. These boundary conditions return the same overall elastic properties than PBC for an orthotropic microstructure. Nevertheless, the Hill condition is not fully satisfied in the case of SiC/SiC VEs, and the computation of the apparent stiffness tensor using the mechanical method defined in equation (6) leads to a slightly non symmetric tensor. So it is necessary to use the energetic definition (equation (7)) which ensures the perfect symmetry of $\boldsymbol{C}^{app}$. Note that differences between these two estimates are very small.

To summarize, the apparent behavior is determined by the finite elements method (using one layer of prismatic elements in the finite element code Cast3m[2]) using the energetic approach and applying KUBC, PBC and the set of MBC proposed by (Pahr and Zysset, 2008). In order to apply periodicity conditions on the non-periodic mesh, linear relationships were implemented between nodes on boundary faces and projected nodes on the opposite faces. Moreover, in all cases, PBC were applied on the two faces of the VE which are perpendicular to the fibers direction for all loading cases. This last option preserves the status of bounds to the apparent stiffness tensor obtained with KUBC prescribed on the other faces.

3. Numerical results : mechanical properties

The elastic behavior of VEs is computed using the finite element meshes described in the above section. The Mandell-Voigt matrix notation in an orthonormal basis will be used to represent the stiffness tensor $\boldsymbol{C}$ (where the direction 3 is coaxial to the fibers direction, see Figure 5):

$$\boldsymbol{\sigma} = \boldsymbol{C}:\boldsymbol{\varepsilon} \Leftrightarrow \begin{pmatrix} \sigma_{11} \\ \sigma_{22} \\ \sigma_{33} \\ \sqrt{2}\sigma_{12} \\ \sqrt{2}\sigma_{13} \\ \sqrt{2}\sigma_{23} \end{pmatrix} = \begin{pmatrix} C_{11} & C_{12} & C_{13} & C_{14} & C_{15} & C_{16} \\ & C_{22} & C_{23} & C_{24} & C_{25} & C_{26} \\ & & C_{33} & C_{34} & C_{35} & C_{36} \\ & sym & & C_{44} & C_{45} & C_{46} \\ & & & & C_{55} & C_{56} \\ & & & & & C_{66} \end{pmatrix} \begin{pmatrix} \varepsilon_{11} \\ \varepsilon_{22} \\ \varepsilon_{33} \\ \sqrt{2}\varepsilon_{12} \\ \sqrt{2}\varepsilon_{13} \\ \sqrt{2}\varepsilon_{23} \end{pmatrix} \qquad (17)$$

3.1. Fluctuations and homogeneous equivalent behavior

3.1.1. Apparent behavior fluctuations

As mentioned above, the homogeneous equivalent behavior of the mechanical RVE must meet some criteria: independence from statistical realization and boundary conditions, and stability relative to the VE size. Moreover, to be valid at the upper scale within an architected composite composed of woven tows, this equivalent behavior should only be used if the size of the mechanical RVE is far smaller than the size of the tows. In order to discuss this RVE question, the apparent behavior was computed for a large number of random square VEs with five increasing sizes. VE characteristics (size, number and surface fractions) for each size are reported in Table 2. VE sizes are compared to fibers and tow sizes through $\delta = L/\bar{R}$ and

---

[2] Finite Element code developed by CEA, http://www-cast3m.cea.fr.

$\alpha = L^2/A_{tow}$, where L is the VE side length, $\bar{R}$ is the mean fiber radius and A_{tow} is the average section of the six observed tows (excluding peripheral matrix).

Size	δ	L [µm]	α	N_R	S_f [%]	S_p [%]
1	5	32.5	0.02	250	64.1	6.68
2	8	52	0.05	200	64.0	6.50
3	15	97.5	0.16	150	64.1	6.41
4	30	192	0.61	53	63.8	6.65
5	40	260	1.13	18	63.6	6.71

Table 2 : Characteristics of generated VEs, where N_R stands for the number of random VEs.

Fluctuations of $\boldsymbol{C}^{app}$ were studied for the five VE sizes using the three types of boundary conditions defined in section 2.3.3. For the sake of clarity, we focus in Figure 6 on the first coefficient of the apparent stiffness tensor C_{11}^{app}. Probability density functions show a very large distribution of C_{11}^{app} for the first three sizes (δ from 5 to 15), with a RSD larger than 10% for all boundary conditions. Distributions become narrower and boundary conditions discrepancies become smaller for larger VEs (fluctuations are less pronounced using KUBC). Most of other tensor coefficients relative to transverse loading conditions exhibit fluctuations similar to that of C_{11}^{app}, with RSDs that decrease from more than 20 % to 6% from size #1 (δ=5) to size #5 (δ=40) using PBC (which exhibit the largest fluctuations).

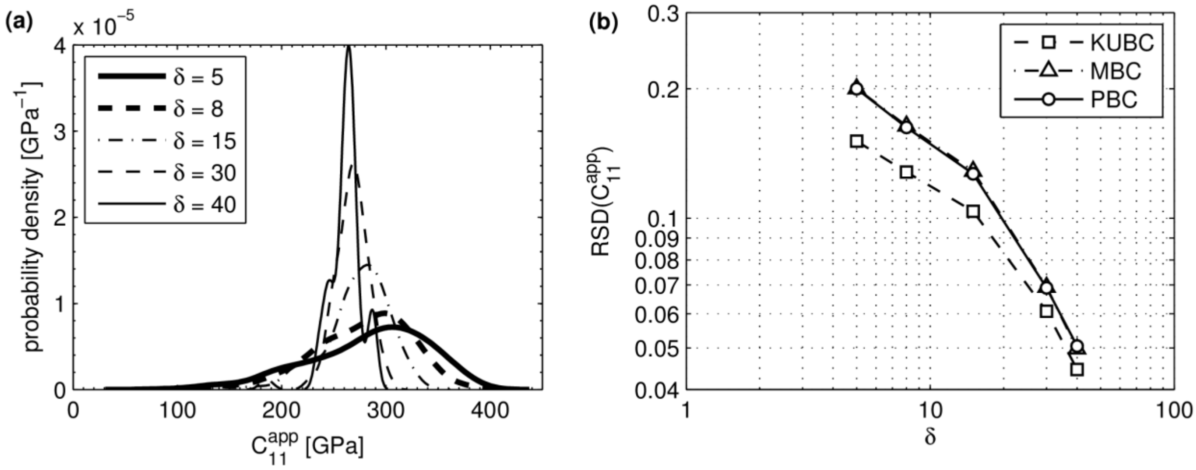

Figure 6 : Fluctuations of C_{11}^{app} for different VE sizes: (a) probability density functions for PBC and (b) evolution of RSD for the three types of boundary conditions.

Although apparent behavior fluctuations are less marked for VEs of sizes #4 and #5, they do not obviously satisfy the criterion of separable scales: these VEs appear to be large (α ~1) compared to the tow size. On the contrary, the two smallest VEs (δ=5 and δ=8) are probably small enough to allow the use of a homogeneous equivalent behavior, but their apparent behavior are depending of the statistical realization too much. Thus, the RVE is too large in comparison to the tow and a homogeneous equivalent behavior based on standard elastic stress-strain relations cannot be rigorously defined at the scale of the tows.

3.1.2. Homogeneous equivalent behavior estimate

How to take these fluctuations into account in structural computation at the scale of the woven composite is still an open issue. As a first approximation, in view of a quantification of the effect of porosity on the elastic behavior, these fluctuations are not considered and the analysis is restricted to the homogeneous equivalent behavior of larger tows. The latter is evaluated by averaging the apparent behaviors of several VEs smaller than the RVE. Such volumes are called Statistical Volume Elements (SVEs). One SVE takes heed of a part of the heterogeneity of the random nature of the microstructure (Ostoja-Starzewski, 2006; Yin et al., 2008). The use of VEs smaller than the RVE has to be offset by averaging the apparent behavior of several SVEs. In such a case, the homogeneous equivalent behavior is bounded by the average over a large number of configurations of SVEs apparent behaviors associated with SUBC and KUBC (Huet, 1990) (equation (18)).

$$\overline{\boldsymbol{S}^{app}_{SUBC}}^{-1} \leq \boldsymbol{C}^{eff} \leq \overline{\boldsymbol{C}^{app}_{KUBC}} \tag{18}$$

Thus, estimates of the effective behavior are obtained from averaging the apparent behavior of several SVEs. Here, only the upper bound can be computed using KUBC, together with estimates provided by MBC and PBC. It has been highlighted that the average value given by any boundary condition may lead to a different estimate than the one obtained from the RVE if the SVEs are too small (Kanit et al., 2003; Ostoja-Starzewski, 1998). In fact, Figure 7a shows that the average $\overline{C_{11}}$ of apparent coefficients C_{11}^{app} depends on both size of the SVEs and boundary conditions. This dependency is quantified using the two indicators Δ_{BC} and $\mathit{\Delta}_{\delta=40}$ defined for each coefficient $\overline{C_{ij}}$ and for a given size δ as

$$\Delta_{BC}(\delta) = \frac{\overline{C_{ij}}(BC) - \overline{C_{ij}}(PBC)}{\overline{C_{ij}}(PBC)}\text{ , with } BC = KUBC \text{ or } MBC \tag{19a}$$

$$\mathit{\Delta}_{\delta=40}(\delta) = \frac{\overline{C_{ij}}(\delta) - \overline{C_{ij}}(\delta = 40)}{\overline{C_{ij}}(\delta = 40)}\text{, using PBC.} \tag{19b}$$

Firstly, we note that $\overline{C_{11}}$ gets larger when SVEs get smaller, whatever the BC, (with discrepancies up to 8% between extreme sizes) and so does the discrepancy between boundary conditions. The latter is significant between the upper bound (KUBC) and the two other estimates, PBC and MBC, which lead to very similar results. But Δ_{KUBC} gets below 3% from $\delta = 30$, corresponding to a less pronounced size effect (with $\mathit{\Delta}_{\delta=40}$<2%).

Secondly, SVE size and boundary conditions have consequences on the number of realizations necessary for the average to converge as illustrated in Figure 7b. $\overline{C_{11}}$ has been computed considering all SVEs available for each size (see Table 2), but less are needed for $\overline{C_{11}}$ to converge, i.e. to remain within a ±2% confidence interval. This number has been estimated for several permutations of SVEs order (about as many permutations as the number N_R of SVEs), leading to the average number of SVEs $\rho_{2\%}$. Thus, $\rho_{2\%}$ naturally decreases when δ increases, down to a few realizations only for size #5., The effect of boundary conditions on the rate of convergence of $\overline{C_{11}}$ becomes insignificant from $\delta = 30$, consistently with the reduced size and boundary conditions effects on $\overline{C_{11}}$.

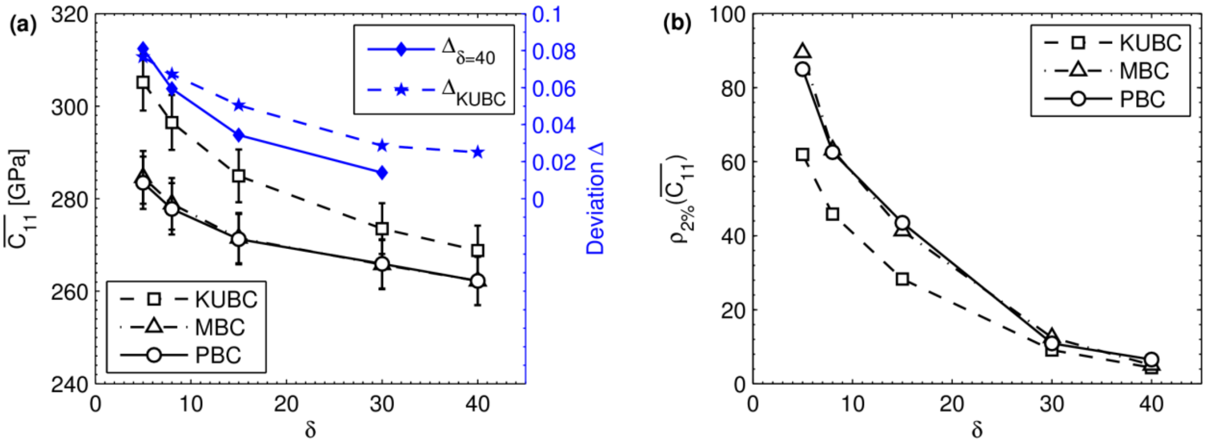

Figure 7 : (a) Evolution of $\overline{C_{11}}$ over SVE sizes for the different BCs, deviation of KUBC results compared with PBC results (Δ_{KUBC}) and deviation relative to size #5 ($\Delta_{\delta=40}$) in blue. Errorbars stand for the ±2% confidence interval of the average. Δ_{MBC} is not reported because it nearly is zero. (b) Mean number of realizations necessary for the average behavior to converge (with a confidence interval of 2%).

The same trend is observed for all coefficients of the transversely isotropic averaged stiffness tensor (note that $\boldsymbol{C}^{app}$ exhibits a monoclinic symmetry, but C_{14}, C_{24}, C_{34} and C_{56} are null on average). Their values using size #4 SVEs are reported in Table 3 along with indicators of size and boundary conditions effects. As might be expected, coefficients relative to the mechanical response in the transverse plane ($\overline{C_{11}}$, $\overline{C_{22}}$, $\overline{C_{12}}$, $\overline{C_{13}}$, $\overline{C_{23}}$ and $\overline{C_{44}}$) converge slower and are more sensitive to SVE size and boundary conditions. In particular, differences are slightly more marked for the shear modulus $\overline{C_{44}}$. But above all, we note that the differences between boundary conditions are so low (<4%) that the estimate obtained using PBC (or MBC) is close enough to the upper bound to be satisfactory. Moreover, using size #5 SVEs would lead to less than 3% discrepancy, which is good enough considering the typical accepted tolerance on $\overline{\boldsymbol{C}}$ variations (~2%). Note finally that transverse isotropy relations ($\overline{C_{11}} = \overline{C_{12}} + \overline{C_{44}}$) are obeyed with a 0.5% error level.

		$\overline{C_{11}}$	$\overline{C_{22}}$	$\overline{C_{33}}$	$\overline{C_{44}}$	$\overline{C_{55}}$	$\overline{C_{66}}$	$\overline{C_{12}}$	$\overline{C_{13}}$	$\overline{C_{23}}$
$\overline{\boldsymbol{C}}(PBC)$	[GPa]	265.9	265.3	366.1	207.9	244.2	244.2	57.59	58.23	58.12
$\rho_{2\%}$	-	13	12	2	12	6	5	12	12	11
$\Delta_{\delta=40}$	[%]	1.4	1.3	0.14	1.5	0.7	0.8	2.4	1.6	1.5
Δ_{KUBC}	[%]	2.9	3.1	0.2	3.7	1.1	1.2	1.4	2.6	2.8
Δ_{MBC}	[%]	0.1	0.3	0	2.9	0.6	0.4	1.2	0.3	0

Table 3 : Results for the homogeneous equivalent behavior estimate with size #4 SVEs (δ=30, mean coefficients are computed over the 53 SVEs). $\rho_{2\%}$ takes the highest value estimated from all three boundary conditions.

Thus, the averaging method leads to a satisfactory estimate of the homogeneous equivalent behavior when using at least about fifteen size #4 SVEs ($\delta = 30$) loaded through PBC (or MBC). These computational conditions will be used for the investigation of the effect of porosity and pore shape in the last part of the paper. About 10 SVEs of size #5 ($\delta = 40$) would also have been sufficient, but size #4 meshes are easier and faster to compute.

3.2. Effects of porosity on the macroscopic and local transverse behavior

3.2.1. Morphology

The porosity is responsible for the anisotropic behavior of SiC/SiC tows within composites elaborated by CVI. In fact, the evolution of the apparent Young modulus as a function of the tensile direction presented in Figure 8a shows that a tensile load leads to a significant loss of stiffness when it is not parallel to the fiber and porosity direction (i.e. direction 3, $\theta = 90°$). A tension in the transverse plane ($\theta = 0°$) involves a 30% decrease of the apparent Yong modulus.

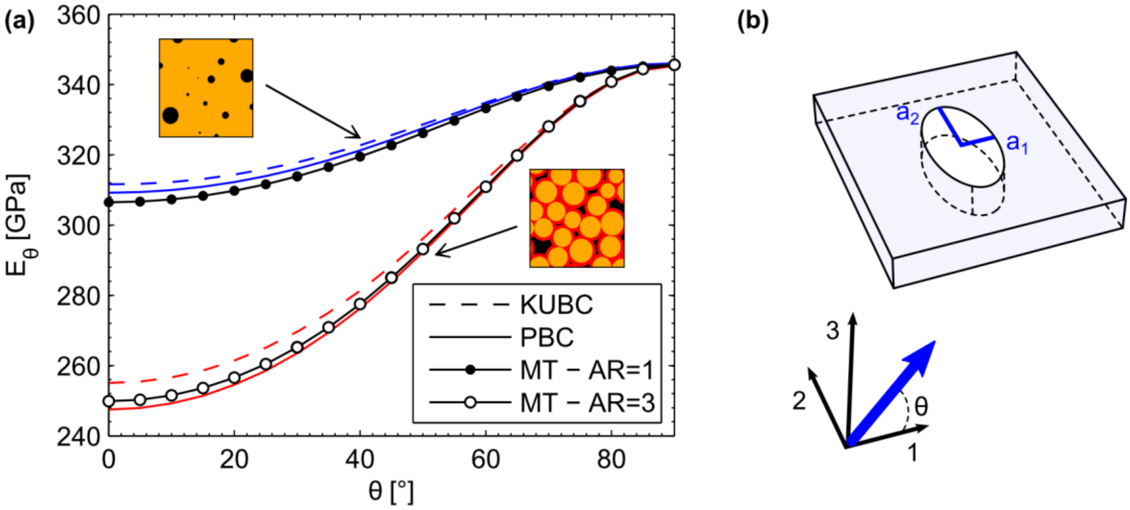

Figure 8 : (a) Apparent Young modulus for a tensile load in the plane (13) versus the angle θ between the tensile direction and direction 1. Mean behaviors over 25 SVEs of CVI microstructure (in red) and cylindrical porous microstructure (in blue) are compared to Mori-Tanaka (MT) estimates (in black); (b) Geometry of pore used in Mori-Tanaka model (same orientation for all pores).

In order to emphasize the contribution of the specific morphology of the porosity to this behavior, this result has been compared to the behavior of a microstructure containing pores whose geometry is simpler. To do so, a microstructure with cylindrical pores with circular cross-section was generated. These pores transverse section exactly has both the same barycenter and the same area than pores in the corresponding CVI microstructure. The homogeneous equivalent behavior was evaluated by averaging the apparent behavior of 25 SVEs. SiC fibers and matrix have a low elastic contrast, so they are simulated by a unique homogeneous isotropic matrix with a Young modulus of 370 GPa (following a simplified mixture law) and a Poisson's ratio of 0.18. Moreover, a classical analytical approach following Mori-Tanaka model, as detailed in (Huang and Talreja, 2005), was used assuming cylindrical pores with elliptical cross section (aspect ratio AR=a_2/a_1, see Figure 8b) with a 6.6% porosity fraction. All results are presented together in Figure 8a.

First of all, the anisotropy induced by porosity clearly is more important with the CVI porosity morphology. The fall in the modulus in the transverse plane is three times as large (30% instead of 10%) for the CVI microstructure as the one with cylindrical pores with circular cross section. Then, the homogeneous equivalent behavior estimated using the Mori-Tanaka analytical approach assuming AR=1 is very close to the one obtained using the numerical model with the circular pores. It confirms the accuracy of Mori-Tanaka model to simulate the elastic behavior of such kind of microstructure (parallel cylindrical pores with circular cross section at low volume fractions – note that this estimate can be shown to coincide with a Hashin-Shtrikman-type lower bound). Moreover, the apparent Young modulus was compared to the Mori-Tanaka estimate for higher aspect ratios, where the minor axis of the elliptical section is parallel to direction 1 (for all pores). Elliptical cylindrical pores with AR=3 are necessary to get similar results than the CVI simulated microstructure. Thus, the CVI morphology is responsible for a fall in the modulus that is equivalent to very elongated and unfavorably oriented ellipse cylindrical pores. Such effect should not be neglected. Note that the latter Mori-Tanaka model used here is not transversely isotropic and is not suitable to account for the CVI porosity. It is only introduced here for comparison purposes. These results are in agreement with previous works that analytically show that the compliance of a concave pore with sharp corners is significantly higher than a convex one with smoother corners (Kachanov et al., 1994). This has been confirmed for 3D pores (Sevostianov and Giraud, 2012), for which concavity has a much stronger impact on elastic properties than ellipticity.

Finally, as illustrated in Figure 8, the boundary conditions effect is less pronounced with the simple shape pores. As shown in Table 4, only a 1% difference is observed for the most affected coefficient $\overline{C_{44}}$ between KUBC and PBC. Fluctuations of the apparent behavior are also far reduced.

			C_{11}			C_{44}	
		CVI	Circular	Circular	CVI	Circular	Circular
δ	-	30	30	8	30	30	8
$\overline{\boldsymbol{C}}$	[GPa]	266	337	339	208	257	258
RSD($\boldsymbol{C}^{app}$)	[%]	5.5	1.6	6.9	3.8	1.9	8.2
Δ_{KUBC}	[%]	2.9	0.6	1.8	3.7	1.1	3.5

Table 4 : Average value, fluctuations (RSD) and discrepancy between PBC and KUBC of C_{11} *and* C_{44}*, for CVI and circular-cylindrical porous microstructures.* $\overline{\boldsymbol{C}}$ *and RSD are computed using PBC.*

Although it is less pronounced, there is also a size effect for the circular pores microstructure. The apparent behavior of 160 size #2 SVEs ($\delta = 8$) containing circular cylindrical pores was computed. Results concerning $\overline{C_{11}}$ and $\overline{C_{44}}$ are also reported in Table 4. The fluctuations for the smallest size are larger, as well as the discrepancy between boundary conditions. Nevertheless, those effects are far less important than those coming from the CVI microstructure. Moreover, the average behaviors between size #2 and size #4 for cylindrical porosity differ by less than 1%. It appears then that size #2 SVEs would be sufficient to accurately estimate the homogeneous equivalent behavior of such a simpler microstructure.

Therefore, the non-separated scales issues are not only due to the heterogeneous pores distribution. They are essentially increased by the specific CVI porosity morphology, which also strongly intensifies the anisotropy by softening the transverse mechanical properties. This means that a realistic representation of the irregular porosity cannot be avoided.

3.2.2. Volume fraction

The porosity volume fraction – controlled through the matrix thickness deposited by CVI – is representative of the process quality. In order to assess the process impact on the mechanical behavior of the tow, five groups of 21 SVEs (size #4) were generated. Fiber location and diameter were similar from one group to another, the only difference between groups being the matrix thickness. Four thicknesses from 1.5 µm to 2.8 µm were used in addition to the experimentally identified one (2.05 µm) leading to mean porosity fractions ranging from 2.8% to 11.5%. The consequences of the porosity fraction evolution on fluctuations of the apparent behavior are illustrated in Figure 9a for the first coefficient C_{11}, together with the sensitivity of the average behavior to boundary conditions. Thus, issues from non-separated scales are stronger for high porosity volume fractions. RSD and Δ_{KUBC} are at least doubled between 6.6% and 11.5% porosity fractions. So size and number of SVEs necessary to estimate the homogeneous equivalent behavior may increase for high volume fractions of porosity. Nevertheless, the corresponding error on overall transverse properties is supposed to be small enough, compared to their sensitivity to the porosity volume fraction.

The main impact of increasing the porosity fraction is the high softening of the transverse mechanical properties. The latter is quantified in Figure 9a with :

$$\Delta_{S_p=6.6\%} = \frac{\overline{C_{11}}(S_p) - \overline{C_{11}}(S_p = 6.6\%)}{\overline{C_{11}}(S_p = 6.6\%)}, \text{using PBC.} \tag{20}$$

It shows that $\overline{C_{11}}$ linearly decreases as the porosity fraction increases over the studied range: there is an almost 50% stiffness loss from 4% to 9% porosities, which are realistic porosity fractions. As illustrated in Figure 9b, the softening is much greater in the transverse plane, and the anisotropy is strongly accentuated by the increased porosity. Furthermore, an increase in the porosity fraction also implies slight pore shape changes. In the studied porosity range, the concavity tends to be accentuated for low matrix thickness: the average solidity of pores (ratio of area over convex area) linearly decreases from 0.7 ($S_p = 2.8\%$) to 0.62 ($S_p = 11.5\%$). So the porosity fraction effect may partially be mixed with shape effect. These results illustrate the issue of identifying the proper parameters of the microstructure, which should characterize the individual pores in accordance with their contributions to the effective elastic properties. As shown by (Kachanov and Sevostianov, 2005), in most cases, these parameters are non-trivial, especially considering irregular shapes, and they may not only reduce to porosity fraction.

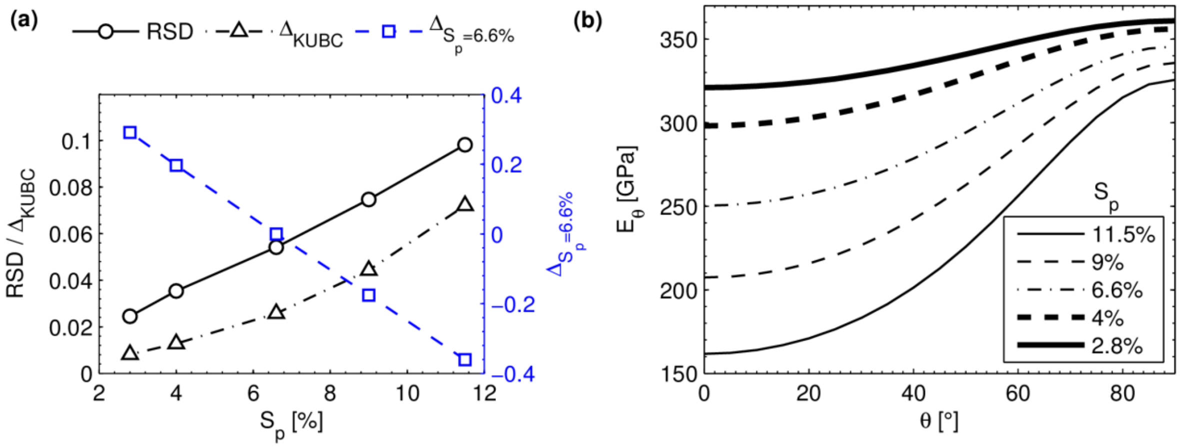

Figure 9 : (a) Fluctuations of C_{11}^{app} (RSD), effects of boundary conditions (Δ_{KUBC}) and porosity volume fraction ($\Delta_{S_p=6.6\%}$) on $\overline{C_{11}}$, and (b) evolution of the mean apparent elastic modulus in the plane (13) as a function of the tensile load direction θ, for five porosity volume fractions using PBC and size #4.

Finally, a decrease in the matrix thickness also modifies the pores pattern and inter-connection: percolation phenomenon may appear as pores are less isolated. The impact of this geometry change on local stress fields are illustrated in Figure 10 and Figure 11, considering a 100 MPa macroscopic tensile test in the transverse plane. Initially (S_p=6.6%), the porosity is responsible for a very heterogeneous and specific local stress distribution, especially in the matrix. Most of local stresses are distributed around 100 MPa, slightly above the macroscopic stress, but another peak around 0 MPa represents areas that are completely unloaded, located on the periphery of large pores (see Figure 11). The tail-end of the distribution beyond 300 MPa corresponds to high stress concentration zones located at the pore singularities. Because fibers are not directly connected to the porosity, their stress distribution is narrow.
These local stress fields are very sensitive to variations of matrix thickness. For the low porosity, stress concentrations are very localized and isolated leading to a relatively uniform stress field. On the contrary, the higher the porosity, the more expanded the stress concentrations. Fibers are then also affected since bands appear in the direction of the traction. This appears together with larger unloaded areas.

In addition to understanding the sensitivity of the elastic properties of the tow to the porosity, the knowledge of local stresses is important to predict damage that initiates in the matrix. Because of very significant effects in the matrix, pore volume fraction is expected to play a key role in the initiation of cracks.

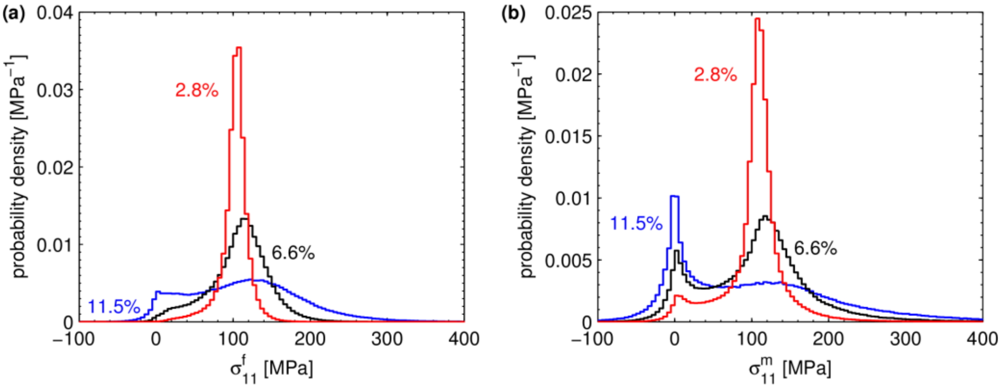

Figure 10 : Mean distributions of σ_{11} in the fibers (σ_{11}^{f}) and in the matrix (σ_{11}^{m}) for a 100 MPa macroscopic tensile test applied along the transverse plane (direction 1), for 3 pore volume fractions (using PBC).

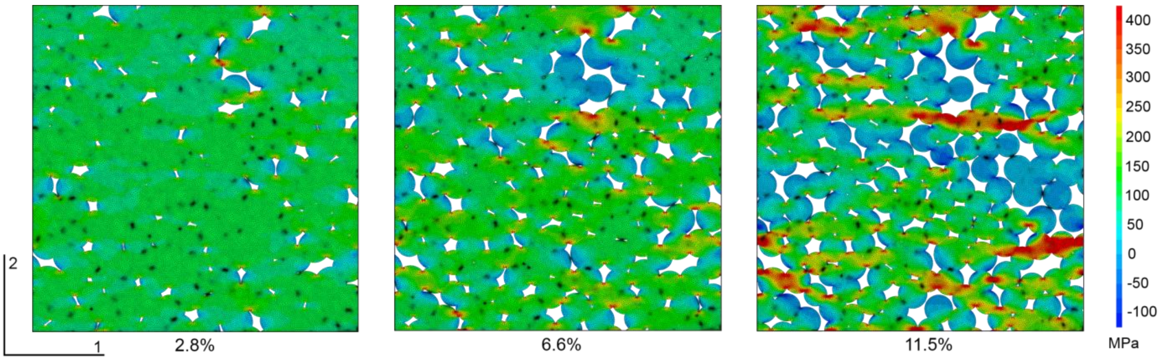

Figure 11 : σ_{11} stress field in a size #4 SVE ($\delta = 30$) for a 100 MPa macroscopic tensile test applied in the transverse plane (direction 1), for 3 porosity volume fractions (using PBC) and identical distribution of fiber centers.

4. Conclusions

The elastic behavior of the tow was studied using the FE simulation of a realistic virtual microstructure. A large number of SVEs were randomly generated on the basis of a significant characterization of the real microstructure. The fiber distribution was validated through statistical descriptors, leading to a heterogeneous distribution of pores which is representative of the residual porosity due to the CVI process. This approach enables to deal with the mechanical RVE issues of such heterogeneous microstructure.

In fact, important fluctuations and sensitivity to boundary conditions of the apparent behavior – even for large SVEs – emphasize an issue of non-separation of scales. Though using a homogeneous equivalent behavior for the tow at the upper scale is questionable, it can be estimated by averaging apparent behaviors of several SVEs. Such SVEs are smaller than the RVE but are large enough to neglect size and boundary conditions effects in average (with ±2 % accuracy). This approach leads to determine that the specific morphology of the residual porosity is responsible for a 30% fall of transverse mechanical properties against longitudinal ones, in addition to an increase of apparent behavior fluctuations. In fact, the softening in the transverse direction is three times as large compared to a simpler material containing cylindrical pores with circular cross-section. Elastic transverse properties and fluctuations are also very sensitive to the porosity volume fraction, which is representative of the quality of the matrix infiltration process. The anisotropy is highly reinforced with the increase of pore volume fraction. Numerical results show an almost 50% stiffness loss in the transverse plane when porosity increases from 4% to 9%. Moreover, the increase of porosity fraction also leads to very heterogeneous stress fields with high stress concentrations, especially in the matrix where cracks are expected to initiate. Thus, a carefully CVI process is necessary to maximize elastic properties of the tow and delay damage initiation in the transverse direction. In addition, and as a future work, the relation between this porosity, which acts as stress concentrators, and the initiation of cracks approximately parallel to the fiber direction, should be deeply studied.

Appendix A. Random generation of fiber positions

Positions of the N_0 fibers (i.e. fiber centers) in the domain A_0 are generated from an initial random distribution of N_0 points, independently of fiber radii. The positions are then rearranged to remove any fiber overlap, using some concepts from the simulation of random close packing of particles (He et al., 1999). This approach was also chosen by (Trias, 2005) in a similar context.

The overlap rate β_{ij}, between the two fibers i and j with position vectors X_i and X_j and radii R_i and R_j, is defined as $\beta_{ij} = (D_{ij}^{min} - d_{ij})/D_{ij}^{min}$. d_{ij} stands for the distance between the fiber centers, and $D_{ij}^{min} = R_i + R_j + e$ is the minimal acceptable distance between these two centers, taking into account a small repulsion distance e. Thus, the overlap rate is positive when the fibers overlap. Until the maximum overlap rate $\beta_{\max}$ over all fibers becomes negative, the fibers positions are rearranged following a relaxation approach (He et al., 1999). The new position X_i^R of a fiber i overlapping n_i neighbor fibers j is given by:

$$X_i^R = \frac{1}{n_i} \sum_{j=1}^{n_i} X_{ij} \tag{A.1}$$

where

$$X_{ij} = X_j + (X_i - X_j) \frac{D_{ij}^{min}}{d_{ij}} \tag{A.2}$$

This new position is accepted only if the new overlap rate stays smaller than $\beta_{\max}$. After the relaxation process, a very small random displacement called vibration is applied to the new fiber positions. The complete arrangement process is achieved following these successive steps while $\beta_{\max} > 0$:

- for $i = 1$ to N_0:
  (1) Determine the overlapping fibers j and the maximum overlap rate $\beta_i = \max(\beta_{ij})$ of the fiber i.
    (a) if $\beta_i > 0$, separate fibers by defining a new position X_i^R (equations (A.1) and (A.2)).
    (b) else the position X_i is unchanged.
  (2) Determine the new maximum overlap rate β_i of the fiber i.
    (a) if $\beta_i > \beta_{\max}$, cancel the displacement and reset the fiber position to X_i.
    (b) else accept the new position, i.e. $X_i = X_i^R$.
- for all fibers whose positions was modified:
  (1) if its coordination number is lower than 4, apply a small random displacement e_V, ie $X_i = X_i + e_V$.
  (2) else the new position is unchanged.

At each arrangement iteration, the fibers sequence is randomized to avoid any bias. Moreover, all fiber centers are restricted to stay in the domain A_0. Any displacement leading to a new position outside A_0 is canceled. Finally, note that it is necessary to define neighboring fibers to improve the efficiency of the algorithm.

Appendix B. Mesh sensitivity

The sensitivity of overall properties to the mesh density was analyzed for a size #4 SVE (δ=30), that was meshed with elements with about 0.5 µm (fine mesh), 1 µm and 1.5 µm (coarse mesh) characteristic lengths. These mesh densities respectively lead to about 3.2e5, 1.1e5 and 0.7e5 elements in the whole SVE. The deviations of the apparent stiffness tensor coefficients from the medium mesh and the coarse mesh, estimated using PBC, are listed in table B.1. The evolution of the deviations is illustrated in figure B.1 together with the effect of boundary conditions.

There is an impact of the mesh density on overall elastic properties, but it is low, considering both PBC and KUBC. The deviations from the medium mesh (1 µm) used in the present study, compared to the finest mesh, are lower than 2% for all coefficients and both BCs. So the mesh sensitivity is limited and too heavy calculations over a very fine mesh are avoided.

		C_{11}	C_{22}	C_{33}	C_{44}	C_{55}	C_{66}	C_{12}	C_{13}	C_{23}
$\boldsymbol{C}_{0.5\,\mu\mathrm{m}}^{app}$	[GPa]	281.0	252.0	366.5	207.6	253.1	238.0	57.8	61.0	55.8
$\Delta_{1\,\mu\mathrm{m}}$	[%]	1.37	1.44	0.05	1.60	0.49	0.56	0.84	1.28	1.33
$\Delta_{1.5\,\mu\mathrm{m}}$	[%]	2.97	3.24	0.1	3.64	1.10	1.30	1.42	2.71	2.90

Table B.1: Apparent stiffness tensor $\boldsymbol{C}_{0.5\,\mu m}^{app}$ of one SVE (size #4) estimated using PBC and the finest mesh, and deviations of coefficients estimated with the medium mesh ($\Delta_{1\,\mu m}$) and the coarse mesh ($\Delta_{1.5\,\mu m}$) compared to $\boldsymbol{C}_{0.5\,\mu m}^{app}$.

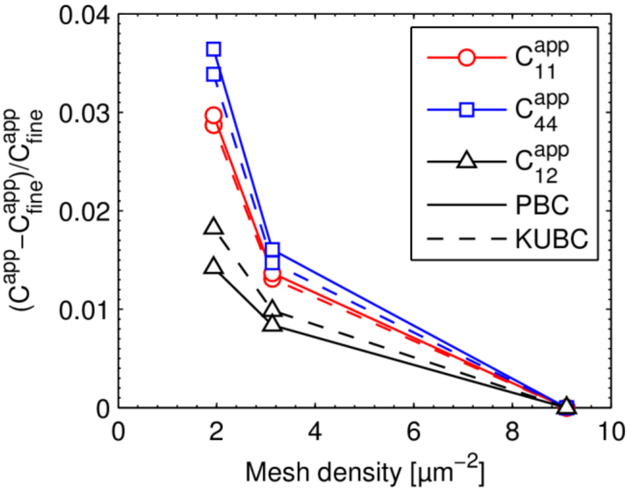

Figure B.1: Evolution of the deviation from the finest mesh of some coefficients of the apparent stiffness tensor of one SVE (size #4) as a function of the mesh density (number of element over the meshed area), using KUBC and PBC. Only the coefficients showing the highest discrepancies between BCs are reported.

References

Aghdam, M.M., Dezhsetan, A., 2005. Micromechanics based analysis of randomly distributed fiber reinforced composites using simplified unit cell model. Compos. Struct. 71, 327–332.

Bornert, M., Bretheau, T., Gilormini, P., 2001. Homogénéisation en mécanique des matériaux. Hermès Science.

Buryachenko, V.A., Pagano, N.J., Kim, R.Y., Spowart, J.E., 2003. Quantitative description and numerical simulation of random microstructures of composites and their effective elastic moduli. Int. J. Solids Struct. 40, 47–72.

Chateau, C., Gélébart, L., Bornert, M., Crépin, J., Boller, E., Sauder, C., Ludwig, W., 2011. In situ X-ray microtomography characterization of damage in SiCf/SiC minicomposites. Compos. Sci. Technol. 71, 916–924.

Chateau, C., Gélébart, L., Bornert, M., Crépin, J., Caldemaison, D., 2010. Multiscale approach of mechanical behaviour of SiC/SiC composites: elastic behaviour at the scale of the tow. Tech. Mech. 30, 45–55.

Chateau, C., Gélébart, L., Bornert, M., Crépin, J., Caldemaison, D., Sauder, C., 2014. Modeling of damage in unidirectional ceramic matrix composites and multi-scale experimental validation on third generation SiC/SiC minicomposites. J. Mech. Phys. Solids 63, 298–319.

Colin, C., Gélébart, L., 2008. Behaviours of SiC fibers and SiC CVI matrix, in: 13th European Congress on Composite Materials, Stockholm.

Deck, C.P., Khalifa, H.E., Sammuli, B., Hilsabeck, T., Back, C.A., 2012. Fabrication of SiC–SiC composites for fuel cladding in advanced reactor designs. Prog. Nucl. Energy 57, 38–45.

Feder, J., 1980. Random Sequential Adsorption. J. Theor. Biol. 87, 237–254.

Gélébart, L., Chateau, C., Bornert, M., Crepin, J., Boller, E., 2010. X-Ray Tomographic Characterization of the Macroscopic Porosity of Chemical Vapor Infiltration SiC/SiC Composites: Effects on the Elastic Behavior. Int. J. Appl. Ceram. Technol. 7, 348–360.

Gélébart, L., Colin, C., 2009. Effects of porosity on the elastic behaviour of CVI SiC/SiC composites. J. Nucl. Mater. 386, 82–85.

Ghosh, S., Nowak, Z., Lee, K., 1997. Quantitative characterization and modeling of composite microstructures by Voronoi cells. Acta Mater. 45, 2215–2234.

Hazanov, S., 1998. Hill condition and overall properties of composites. Arch. Appl. Mech. 68, 385–394.

Hazanov, S., Amieur, M., 1995. On Overall Properties Of Elastic Heterogeneous Bodies Smaller Than The Representative Volume. Int. J. Eng. Sci. 33, 1289–1301.

Hazanov, S., Huet, C., 1994. Order Relationships For Boundary-Conditions Effect In Heterogeneous Bodies Smaller Than The Representative Volume. J. Mech. Phys. Solids 42, 1995–2011.

He, D., Ekere, N.N., Cai, L., 1999. Computer simulation of random packing of unequal particles. Phys. Rev. E 60, 7098–7104.

Hinrichsen, E.L., Feder, J., Jossang, T., 1986. Geometry Of Random Sequential Adsorption. J. Stat. Phys. 44, 793–827.

Hironaka, K., Nozawa, T., Hinoki, T., Igawa, N., Katoh, Y., Snead, L.L., Kohyama, A., 2002. High-temperature tensile strength of near-stoichiometric SiC/SiC composites. J. Nucl. Mater. 307, 1093–1097.

Huang, H., Talreja, R., 2005. Effects of void geometry on elastic properties of unidirectional fiber reinforced composites. Compos. Sci. Technol. 65, 1964–1981.

Huet, C., 1990. Application Of Variational Concepts To Size Effects In Elastic Heterogeneous Bodies. J. Mech. Phys. Solids 38, 813–841.

Igawa, N., Taguchi, T., Nozawa, T., Snead, L.L., Hinoki, T., McLaughlin, J.C., Katoh, Y., Jitsukawa, S., Kohyama, A., 2005. Fabrication of SiC fiber reinforced SiC composite by chemical vapor infiltration for excellent mechanical properties. J. Phys. Chem. Solids 66, 551–554.

Jodrey, W.S., Tory, E.M., 1985. Computer-Simulation Of Close Random Packing Of Equal Spheres. Phys. Rev. A 32, 2347–2351.

Kachanov, M., Sevostianov, I., 2005. On quantitative characterization of microstructures and effective properties. Int. J. Solids Struct. 42, 309–336.

Kachanov, M., Tsukrov, I., Shafiro, B., 1994. Effective moduli of solids with cavities of various shapes. Appl. Mech. Rev. 47, S151–S174.

Kanit, T., Forest, S., Galliet, I., Mounoury, V., Jeulin, D., 2003. Determination of the size of the representative volume element for random composites: statistical and numerical approach. Int. J. Solids Struct. 40, 3647–3679.

Katoh, Y., Snead, L.L., Henager, C.H., Hasegawa, A., Kohyama, A., Riccardi, B., Hegeman, H., 2007. Current status and critical issues for development of SiC composites for fusion applications. J. Nucl. Mater. 367, 659–671.

Keleş, Ö., García, R.E., Bowman, K.J., 2013. Stochastic failure of isotropic, brittle materials with uniform porosity. Acta Mater. 61, 2853–2862.

Knight, M.G., Wrobel, L.C., Henshall, J.L., 2003. Micromechanical response of fibre-reinforced materials using the boundary element technique. Compos. Struct. 62, 341–352.

Maligno, A.R., Warrior, N. a., Long, A.C., 2009. Effects of inter-fibre spacing on damage evolution in unidirectional (UD) fibre-reinforced composites. Eur. J. Mech. - A/Solids 28, 768–776.

Matsuda, T., Ohno, N., Tanaka, H., Shimizu, T., 2003. Effects of fiber distribution on elastic-viscoplastic behavior of long fiber-reinforced laminates. Int. J. Mech. Sci. 45, 1583–1598.

Melro, A.R., Camanho, P.P., Pinho, S.T., 2008. Generation of random distribution of fibres in long-fibre reinforced composites. Compos. Sci. Technol. 68, 2092–2102.

Melro, A.R., Camanho, P.P., Pinho, S.T., 2012. Influence of geometrical parameters on the elastic response of unidirectional composite materials. Compos. Struct. 94, 3223–3231.

Michaux, A., Sauder, C., Camus, G., Pailler, R., 2007. Young's modulus, thermal expansion coefficient and fracture behavior of selected {Si-B-C} based carbides in the 20-1200 degrees C temperature range as derived from the behavior of carbon fiber reinforced microcomposites. J. Eur. Ceram. Soc. 27, 3551–3560.

Naslain, R., 2004. Design, preparation and properties of non-oxide CMCs for application in engines and nuclear reactors: an overview. Compos. Sci. Technol. 64, 155–170.

Nolan, G.T., Kavanagh, P.E., 1993. Computer-Simulation Of Random Packings Of Spheres With Log-Normal Distributions. Powder Technol. 76, 309–316.

Novak, J., Tsukrov, I., Piat, R., Schnack, E., 2002. On contribution of pores into the effective elastic properties of carbon/carbon composites. Int. J. Fract. 118, 31–36.

Oh, J.H., Jin, K.K., Ha, S.K., 2006. Interfacial Strain Distribution of a Unidirectional Composite with Randomly Distributed Fibers under Transverse Loading. J. Compos. Mater. 40, 759–778.

Ostoja-Starzewski, M., 1998. Random field models of heterogeneous materials. Int. J. Solids Struct. 35, 2429–2455.

Ostoja-Starzewski, M., 2006. Material spatial randomness: From statistical to representative volume element. Probabilistic Eng. Mech. 21, 112–132.

Pahr, D.H., Zysset, P.K., 2008. Influence of boundary conditions on computed apparent elastic properties of cancellous bone. Biomech. Model. Mechanobiol. 7, 463–476.

Pyrz, R., 1994a. Quantitative Description Of The Microstructure Of Composites .1. Morphology Of Unidirectional Composite Systems. Compos. Sci. Technol. 50, 197–208.

Pyrz, R., 1994b. Correlation Of Microstructure Variability And Local Stress-Field In 2-Phase Materials. Mater. Sci. Eng. A-Structural Mater. Prop. Microstruct. Process. 177, 253–259.

Ripley, B.D., 1977. Modelling Spatial Patterns. J. R. Stat. Soc. Ser. B 39, 172–212.

Romanov, V., Lomov, S. V., Swolfs, Y., Orlova, S., Gorbatikh, L., Verpoest, I., 2013. Statistical analysis of real and simulated fibre arrangements in unidirectional composites. Compos. Sci. Technol. 87, 126–134.

Romanowicz, M., 2010. Progressive failure analysis of unidirectional fiber-reinforced polymers with inhomogeneous interphase and randomly distributed fibers under transverse tensile loading. Compos. Part A Appl. Sci. Manuf. 41, 1829–1838.

Salmi, M., Auslender, F., Bornert, M., Fogli, M., 2012. Apparent and effective mechanical properties of linear matrix-inclusion random composites: Improved bounds for the effective behavior. Int. J. Solids Struct. 49, 1195–1211.

Sauder, C., Lamon, J., 2007. Tensile creep behavior of SiC-based fibers with a low oxygen content. J. Am. Ceram. Soc. 90, 1146–1156.

Segurado, J., Llorca, J., 2002. A numerical approximation to the elastic properties of sphere-reinforced composites. J. Mech. Phys. Solids 50, 2107–2121.

Sevostianov, I., Giraud, A., 2012. On the Compliance Contribution Tensor for a Concave Superspherical Pore. Int. J. Fract. 177, 199–206.

Sha, J.J., Nozawa, T., Park, J.S., Katoh, Y., Kohyama, A., 2004. Effect of heat treatment on the tensile strength and creep resistance of advanced SiC fibers. J. Nucl. Mater. 329-333, 592–596.

Trias, D., 2005. Analysis and simulation of transverse random fracture of long fiber reinforced composites. University of Girona.

Trias, D., Costa, J., Mayugo, J.A., Hurtado, J.E., 2006. Random models versus periodic models for fibre reinforced composites. Comput. Mater. Sci. 38, 316–324.

Tsukrov, I., Novak, J., 2002. Effective elastic properties of solids with defects of irregular shapes. Int. J. Solids Struct. 39, 1539–1555.

Vaughan, T.J., McCarthy, C.T., 2010. A combined experimental-numerical approach for generating statistically equivalent fibre distributions for high strength laminated composite materials. Compos. Sci. Technol. 70, 291–297.

Widom, B., 1966. Random Sequential Addition Of Hard Spheres To A Volume. J. Chem. Phys. 44, 3888–3894.

Wongsto, A., Li, S., 2005. Micromechanical FE analysis of UD fibre-reinforced composites with fibres distributed at random over the transverse cross-section. Compos. Part A-Applied Sci. Manuf. 36, 1246–1266.

Yang, A., Miller, C.T., Turcoliver, L.D., 1996. Simulation of correlated and uncorrelated packing of random size spheres. Phys. Rev. E 53, 1516–1524.

Yin, X.L., Chen, W., To, A., McVeigh, C., Liu, W.K., 2008. Statistical volume element method for predicting micro structure-constitutive property relations. Comput. Methods Appl. Mech. Eng. 197, 3516–3529.

Zeman, J., Sejnoha, M., 2001. Numerical evaluation of effective elastic properties of graphite fiber tow impregnated by polymer matrix. J. Mech. Phys. Solids 49, 69–90.